

Light-Induced Plasmon-Assisted Phase Transformation of Carbon on Metal Nanoparticles

Dhaval D. Kulkarni, Songkil Kim, Andrei G. Fedorov, and Vladimir V. Tsukruk*

Highly localized light-induced phase transformation of electron beam induced deposited carbon nanostructures (dots and squares) on noble metal surfaces is reported. The phase transformation from the amorphous phase to the disordered graphitic phase is analyzed using the characteristic Raman signatures for amorphous and graphitized carbon and conductive force microscopy. The extent of the transformation is found to be largely dependent on the plasmon absorption properties of the underlying metal film. It is observed that the amorphous carbon deposits on the silver films consisting of 12 nm particles with the plasmon absorption near the laser excitation wavelength (514 nm), undergo fast graphitization to a nanocrystalline or a disordered graphitic phase. This transformation results in the formation of a highly conductive carbon/metal interface with at least seven orders of magnitude lower electrical resistivity than the initial insulating interface. It is suggested that the fast graphitization of nanoscale carbon deposits might serve as an efficient path for the formation of complex patterned nanoscale metal-carbon interconnects with high electrical conductivity.

1. Introduction

Light-induced transformation of materials is a common phenomenon observed in our day-to-day life for generating energy to sustain life processes.^[1,2] Over the years, studies on light-matter interactions have led to the discovery of many light-induced reactions such as photoisomerization,^[3] photopolymerization,^[4] and photoionization^[5]. Also, light-based phenomena, such as the photoelectric effect,^[6] photomagnetic effect,^[7] photoacoustic effect,^[8] and photothermal effect,^[9] have made their way into many device applications. In fact, photothermal phenomena at the nanoscale have been studied in the efforts to develop and control biochemical reactions,^[10,11,12,13] induce photomechanical actuation,^[14] manipulate the precise growth of nanostructures,^[15] improve the efficiency of heterogeneous catalysis,^[16,17] and for therapeutic applications.^[18,19] This area can also open up opportunities to bring about controlled

and localized heating with nanoscale precision for inducing confined phase transitions in different materials, such as patterning graphene oxide with conductive domains.^[20] With the miniaturization of electronic devices, these methods can be used to develop complex phase interconnect architectures for the semiconductor applications.

Electron beam induced deposition (EBID) has been used for the nanoscale growth of amorphous carbon and metals, with complex 2D and 3D geometries.^[21] These deposits can be fabricated over relatively small areas, making it important for nanoscale fabrication of interconnect arrays.^[22,23] In fact, these deposits have been known to act as a good soldering material for improving the mechanical contact between heterogeneous materials (e.g., metal/metal or metal/semiconductor interfaces).^[24] However, as deposited EBID

carbon is amorphous, with significant hydrogen content and low electrical conductivity.^[25] Thus, post-deposition treatment is required for dehydrogenation and directed phase transformation into the electrically conductive graphitic phase for its use as a soldering material in electronic devices.^[26] Amorphous carbon composed of both sp^2 and sp^3 carbon bonds is known for its high chemical stability, optical transparency, and excellent mechanical properties, thereby making it important in areas of protective coatings and optoelectronics.^[27–30] Conductive carbon nanostructures can be achieved by tuning the relative sp^2/sp^3 content and nanostructure morphologies. Different methods have been used to transform amorphous carbon films into graphitic structures. Thermal annealing at high temperatures has been commonly exploited for inducing the formation of electrically conductive graphitic nanostructures.

Recently, we showed that the phase transformation in nanoscale EBID amorphous carbon deposits takes place between 100 and 400 °C.^[23] It has been observed that at lower temperature, stress relaxation and dehydrogenation take place, followed by partial graphitization and formation of a disordered graphitic phase at temperatures above 300 °C. However, these transformations involve subjecting the entire substrate to high temperatures and are relatively slow, thereby limiting their use to several applications including fabrication of electronic devices. As is known, bulk carbon materials can absorb light more efficiently and have been known to ignite or show a strong thermal emission upon excitation.^[31,32] However, nanoscale carbon deposits with sub-micrometer dimensions cannot be directly

D. D. Kulkarni, Prof. V. V. Tsukruk
School of Materials Science and Engineering
Georgia Institute of Technology
Atlanta, GA 30332-0245, USA
E-mail: vladimir@mse.gatech.edu
S. K. Kim, Prof. A. G. Fedorov
Woodruff School of Mechanical Engineering
Georgia Institute of Technology
Atlanta, GA 30332-0245, USA



DOI: 10.1002/adfm.201102665

employed for light-induced transformations because these structures are light transparent and most of the incident light is not absorbed if special designs are not implemented.

One of the approaches is the exploitation of metal nanostructures to induce local heating at metal/carbon interfaces. Indeed, noble metal nanostructures exhibit a strong absorption in the visible region because of the surface plasmon resonances in response to the external electromagnetic radiation.^[33] This strong light absorption causes a local increase in the temperature of the nanoparticles and can increase the rate of photochemical reaction.^[16] Recently, the heat generated by surface plasmons was utilized for bringing about rippling of polymer surfaces and for inducing phase transformations.^[34–36] Brongersma et al. showed a localized photothermal growth of carbon nanotubes and silicon nanowires on metal nanoparticles exposed to a focused light beam.^[15]

Here, we demonstrate a fast and highly localized phase transformation of amorphous carbon deposits on nanoparticulate metal films without global thermal treatment and the subsequent improvements in the deposited carbon's electrical conductivity. We highlight the critical role of surface plasmons excited by the laser source in bringing about a large local increase in the temperature, sufficient to induce graphitization of amorphous carbon deposits and quickly convert them to disordered graphitic phase. The annealing kinetics of the carbon deposits on different metal films clearly demonstrates the role of the substrate on the carbon nanodeposit phase transformation.

In this study, EBID was used to make 0D (dots) and 2D (square) carbon nanostructures on a silicon substrate, a gold film, and a silver film. The change in the composition and microstructure of the deposits on different substrates after exposure to the incident light at 514 nm was evaluated using Raman spectroscopy. Also, the effect of the localized heating on the morphology of the substrate was analyzed using atomic force microscopy (AFM). Furthermore, to confirm the increase in electrical conductivity of these deposits associated with the amorphous to graphitic phase transition, conductive force microscopy (CFM) imaging was used to contrast the enhanced electrical conductivity of regions of the carbon deposits selectively exposed to laser irradiation from the unexposed regions.

2. Results and Discussion

2.1. Metal Nanostructures

Three different common substrates were utilized for this study: silicon (Si) wafer, gold (Au) film, and silver (Ag) film (see Experimental Section). **Figure 1** shows topographical AFM images of these substrates along with their corresponding cross-sections. Bare silicon and gold films appear to be relatively smooth with a root mean square (RMS) microroughness of 0.17 nm and 0.51 nm, respectively, over a surface area of 1 μm^2 (Figure 1a,b). In contrast, silver film shows a significantly rough surface with an RMS roughness of 3.6 nm and dense granular morphology with nanoparticles measured to be 12 ± 0.9 nm in diameter (Figure 1c). The gold film shows the presence of continuous island-like morphology.

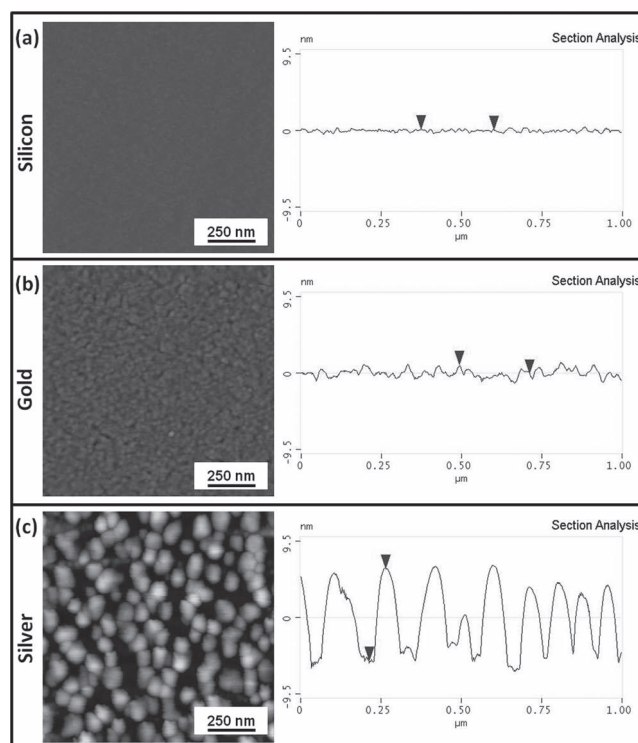
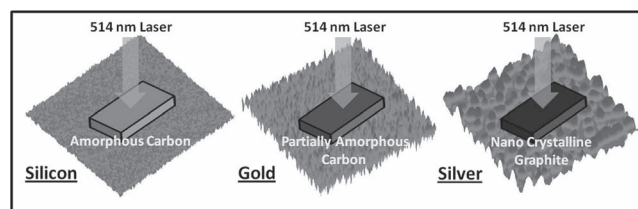


Figure 1. AFM images showing the morphology and sectional analysis of different films: a) silicon substrate, b) gold film, and c) silver film. The z-scale is 20 nm for all the images.

2.2. EBID Deposit Fabrication

After analyzing the surface morphology of different substrates, EBID carbon deposits of similar shapes and sizes were deposited over these substrates (**Scheme 1**). The schematic shows the formation of selected areas with graphitized carbon within carbon films on substrates with different morphologies, as will be discussed in detail. Electron beam focused at a spot for a prolonged period of time leads to the formation of dot-like structures from residual hydrocarbons (“contamination”) as a precursor. Scanning electron microscopy (SEM) images of deposits upon tilting the substrate at 45° with respect to the electron beam reveal a pillar like morphology for the dots (**Figure 2a**). Although the substrate would have an influence on the morphology of the EBID deposits because of the difference in the secondary electron yield and surface diffusion coefficient, the dimensions of the deposits on the different substrates were within ± 200 nm.



Scheme 1. EBID amorphous carbon nanostructures (grey blocks) fabricated on substrates with different composition (silicon, gold, and silver) and surface morphologies and their physical state upon exposure to a 514 nm laser source.

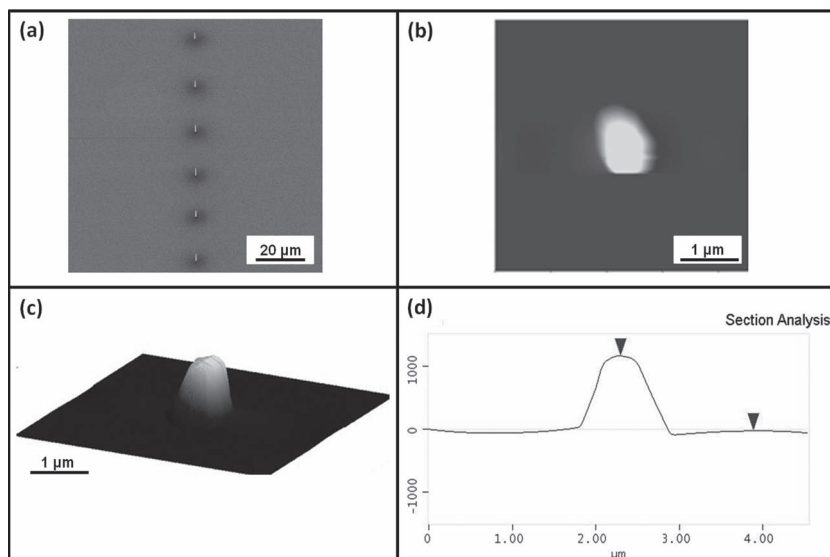


Figure 2. Morphology of the EBID carbon deposit. a) SEM image obtained at 45° viewing showing an array of carbon deposits, b) AFM image of one of the carbon deposit (z-scale: 1.5 μm), c) corresponding 3D image showing its pillar-like morphology (z-scale: 1.5 μm), and d) sectional analysis.

The size and structure of the EBID carbon deposits over different substrates were quantified using AFM imaging. Figure 2b shows the AFM image of the dots along with the corresponding 3D image (Figure 2c) and cross-sectional profile (Figure 2d). 3D image of the dots also reveals a pillar-like morphology in agreement with the SEM image (Figure 2a). The height of the dots is approximately $1.2 \pm 0.2 \mu\text{m}$ and their width is $0.72 \pm 0.15 \mu\text{m}$ for an electron beam exposure time of 10 min. The shape and size of the deposits can be varied by adjusting the SEM deposition settings and exposure time, as has been discussed in detail elsewhere.^[25]

2.3. Phase Composition

The intrinsic physical state of the carbon deposits was analyzed from the Raman spectra collected from individual carbon structures using confocal Raman micromapping under minimum laser power (<1 mW) to avoid any laser-induced heating. All carbon materials show characteristic D-bands and G-bands between $1350\text{--}1380 \text{ cm}^{-1}$ and $1560\text{--}1590 \text{ cm}^{-1}$, respectively, which relate to the sp^2 and sp^3 content of the system.^[37,38] Generally, the Raman spectra of carbon materials are dominated by the sp^2 sites because of their higher scattering cross-section.^[39] Thus, depending on the peak positions and the intensity ratio of these bands, the microstructure of the material can be identified (for detailed discussion, see ref. [23]). Briefly, amorphous and graphitized carbon show G-band peaks around 1520 cm^{-1} and 1580 cm^{-1} , respectively, and increase in the disorder of a graphitized system leads to the breakdown of the large graphitic domains into smaller moieties, thereby further shifting the G-band peak to $1590\text{--}1600 \text{ cm}^{-1}$.^[37] This phase is termed as “nanocrystalline graphite” and represents carbon material with a disordered graphitic microstructure with short-range ordering of graphitic planes.^[40]

Also, it is worth noting that the thermal stresses in the deposits can contribute to a shift in the observed Raman

spectrum. Carbon nanotubes have been known to show a significant shift in their strain sensitive Raman peaks under tensile and compression loadings.^[41,42,43] Typically, the thermal strain in the system can be estimated from the product of the thermal expansion coefficient and the change in temperature. Thus, assuming that the coefficient of thermal expansion of the amorphous carbon deposits is $\approx 3\text{--}5 \mu\text{C}^{-1}$ and the local temperature at the surface to be $\approx 400\text{--}450 \text{ }^\circ\text{C}$, the strain in the deposits can be $\approx 0.12\text{--}0.2\%$.^[44,45] This can result in a shift in the G-band peak position by $\approx 3\text{--}6 \text{ cm}^{-1}$.^[46,47]

Figure 3 shows the high-resolution Raman map and the corresponding Raman scattering obtained from averaging over 400 individual spectra of the EBID carbon dots on different substrates. The images were obtained by integrating the intensity of the peaks between 1000 cm^{-1} and 1800 cm^{-1} to account for the characteristic D-band and G-band peaks for carbon dots. Interestingly, the carbon dots on different substrates showed significantly

different Raman characteristics. The G-band peak position and the D/G ratio of the dots deposited on silicon substrate are approximately $1556 \pm 1 \text{ cm}^{-1}$ and 1.2, respectively (Figure 3a). For carbon deposits on gold film, the G-band peak position is slightly higher than on silicon ($1564.6 \pm 1.5 \text{ cm}^{-1}$) with the D/G ratio of approximately 1.5 (Figure 3b). The slight difference in the G-band peak positions of the carbon dots on silicon and gold substrate may be due to the difference in the internal stresses. These stresses are formed during fabrication due to the difference in the secondary electron yield and surface diffusion coefficient.

In contrast, the Raman spectrum for the carbon deposits on the silver film showed the G-band and D-band peaks completely distinguishable from one another. The G-band peak position for dots deposited on the silver film reached 1582 cm^{-1} (Figure 3c). Also, the D/G ratio is significantly higher (1.9) than the deposits on silicon (1.2) and gold (1.5). This suggests that although the carbon deposits were fabricated under identical conditions, they exhibit different microstructure when exposed to the laser source at 514 nm.

Thus, the analysis of Raman data suggests that as-deposited carbon dots on silicon substrate are partially amorphous with some sp^2 content. However, the deposits on silver film show G-band peak position shifted significantly above 1580 cm^{-1} , implying an increase in the graphitic ordering with the formation of the nanocrystalline carbon phase inside the structure upon laser exposure, a unique phenomenon revealed in this study.

As is known, an amorphous to graphitic transformation usually requires exposure to high temperature or high pressure.^[23,48] However, in this study, the amorphous carbon deposits were subjected to an extremely low laser power (<1 mW) under normal atmospheric conditions. This phenomenon suggests that the substrate must be influencing the phase transformation process of the as-deposited amorphous carbon deposits under laser illumination. In particular, bare silicon

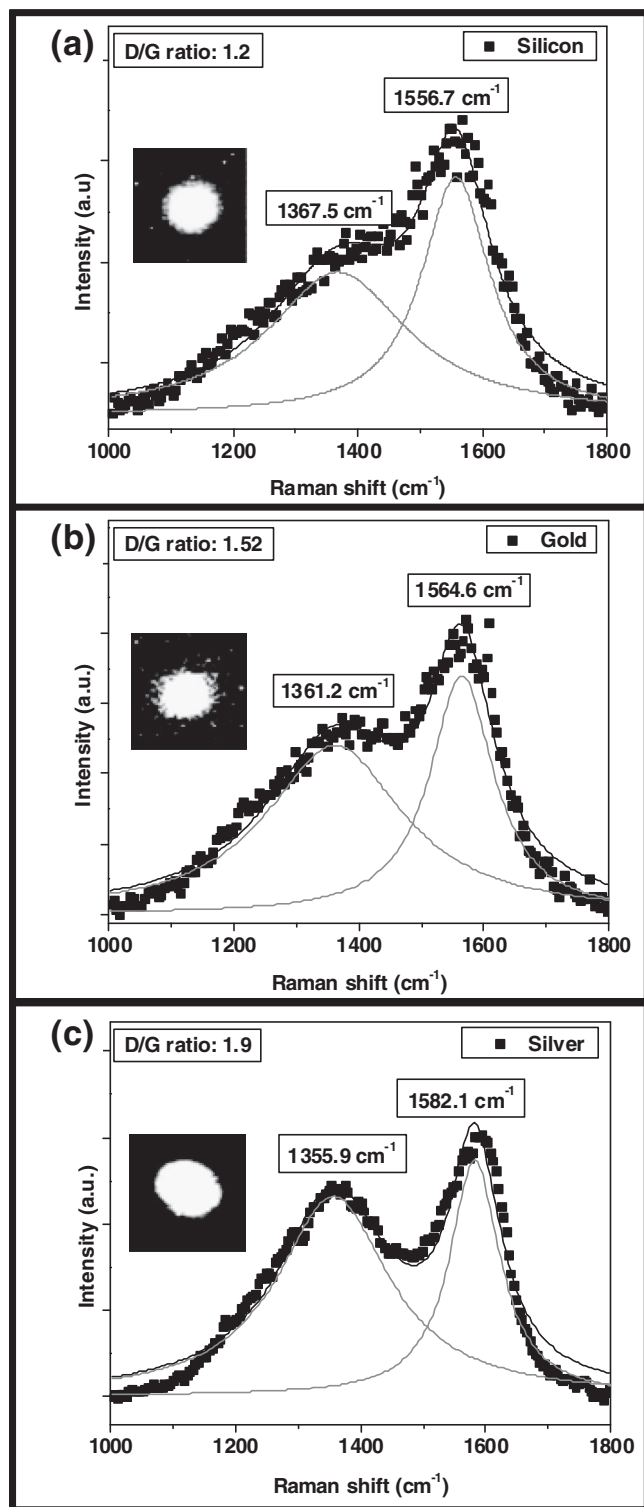


Figure 3. Raman spectra of carbon deposits with insets showing the Raman maps on a) silicon substrate, b) gold film, and c) silver film.

substrate shows no effect on the properties of the amorphous carbon deposits. However, noble metal films seem to influence the characteristics of the as-deposited carbon deposits in the presence of a laser source. Thus, the interaction of light with

the metal film needs to be studied in order to understand the laser-assisted phase transformation.

2.4. Optical Properties of Sputtered Metal Films

Figure 4 represents the refractive indices and extinction coefficients of the gold and silver films used in this study. The gold film showed a slight variation of the refractive index up to 450 nm, followed by a steady decrease with an increase in wavelength (Figure 4a). It shows a near-zero refractive index at wavelengths between 550 and 580 nm and continues to rise thereafter. A similar trend is observed for the silver film (Figure 4b). The refractive index shows a slight variation in the near UV wavelengths followed by a steady decrease, approaching zero between 550 and 580 nm and continues to steadily increase up to 900 nm. These results correlate well with the optical properties of evaporated metal films reported by Sennett et al.^[49] At shorter wavelengths, bound electrons contribute towards the absorption whereas at higher wavelengths, the absorption due to free electrons is more dominant. This transition occurs in the visible region and UV region of the electromagnetic spectrum for gold and silver films, respectively. In the case of gold films, the absorption increases at wavelengths above 550 nm whereas silver film strongly absorbs at all wavelengths.

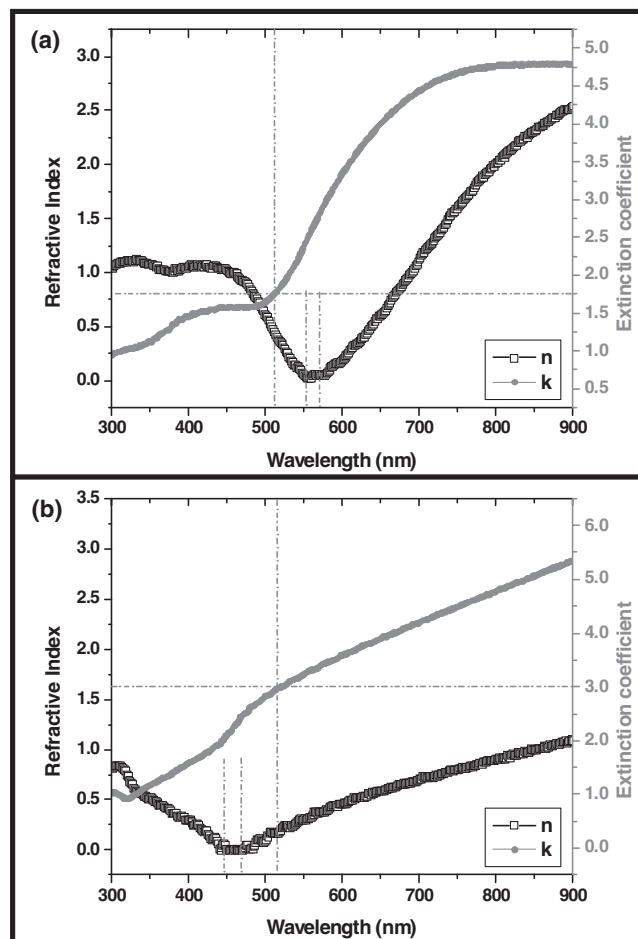


Figure 4. The variation of refractive index (n) and absorption coefficient (k) with wavelength of a) gold film and b) silver film.

Figure 4 also gives the variation of the extinction coefficient of the metal films with the wavelength. The extinction coefficient for the gold film shows an increase up to 500 nm with a small bump around 420 nm and sharply increases up to 700 nm (Figure 4a). Above 700 nm, the extinction coefficient for the gold film saturates. For the silver film, the extinction coefficient shows a near linear increase from 300 nm to 450 nm and undergoes a transition between 450 and 480 nm and continues to linearly increase up to 900 nm (Figure 4b). It is interesting to note that the extinction coefficient of these films shows little variation at wavelengths where the refractive index approaches a minimum.

The sudden drop in the refractive index of the metal films is caused by the free electron transition, which occurs due to the resonant coupling between the surface plasmons and incident electromagnetic wave, and can be described using the Drude model for free electron oscillations.^[50–53] At the resonant frequency, the real part of the permittivity approaches zero and consequently the refractive index approaches zero. A refractive index of less than 1 represents a pure metal-like behavior of the sputtered films. However, these resonances occur at a slightly different wavelength than that of our laser source.

Comparing the absolute values of the extinction coefficient at 514 nm, the absorptive index of silver (3.0) is significantly higher than that for gold (1.75), suggesting that the silver film absorbs light more efficiently than the gold film. Thus, on exposure to the incident light, the surface plasmons of silver nanoparticles oscillate near its resonant frequency and absorb the incident light more efficiently than the gold surface, though the plasmon resonance of gold is also close to the laser wavelength.

Such localized electromagnetic enhancement of light is achieved by excitation of the surface plasmons of metal nanoparticles at or near their resonant frequency.^[54–56] As a result, metal nanoparticles act as nanoheat generators, absorbing incident light and converting it into thermal energy.^[17,57,58,59] This heating effect is especially strong under the plasmon resonance conditions when the energy of the incident photons is close to the plasmon frequency of the metal nanoparticles. Thus, based on the optical properties of metal films discussed above, we suggest that the thermal energy generated by the surface plasmons might be responsible for bringing about the phase transformation of amorphous carbon deposits.

2.5. Effect of Laser Exposure on the Substrate

To further consider the effect of the laser illumination on the metal films, we studied the silver and gold films under identical direct light exposure. Figure 5 shows the topographical AFM images of these exposed areas along with the corresponding phase images. It can be clearly seen that the surface

morphology of the silver film changes significantly in the areas exposed to the laser, whereas the gold film does not show any apparent change in its surface features. A high-resolution AFM image in Figure 6 shows that the nanoparticles within the laser-exposed regions of the silver film became significantly reduced in size, indicating intense changes in silver nanoparticle morphology after exposure to light. The average size of the silver nanoparticles in the exposed areas is 2.3 nm, as compared to 12 nm in the unexposed areas.

Ablation of metal nanostructures using a high powered laser source is well known in the literature.^[60,61,62] However, the laser used in this research is a low-power continuous laser and the power density used in this study is several orders of magnitude (at least four) lower than that reported.^[63] Thus, direct light-induced ablation of the metal nanoparticles is improbable under our experimental conditions. We speculate that the localized excitation of surface plasmons of the silver film that possess absorption near the incident laser frequency causes temperature to dramatically increase in the exposed areas, to a value high enough to affect the surface morphology of the area. Also, it is well established from our previous work that a temperature of around 350–400 °C would be required for the EBID amorphous carbon deposit to graphitize completely. Although the exact temperature at the surface of the nanoparticles on laser exposure is a challenge to measure under the current experimental conditions, an estimate of the temperature required for silver nanoparticle morphology changes would be necessary.

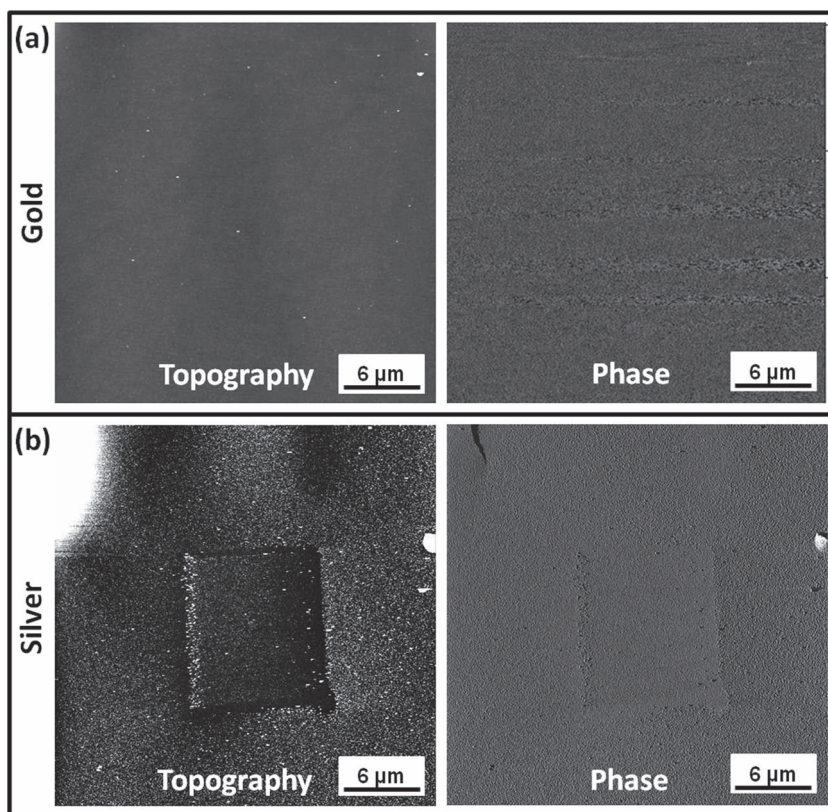


Figure 5. AFM image of the metal films after exposure to the laser showing the topography (z-scale: 20 nm) and phase (z-scale: 60°) of a) gold film and b) silver film.

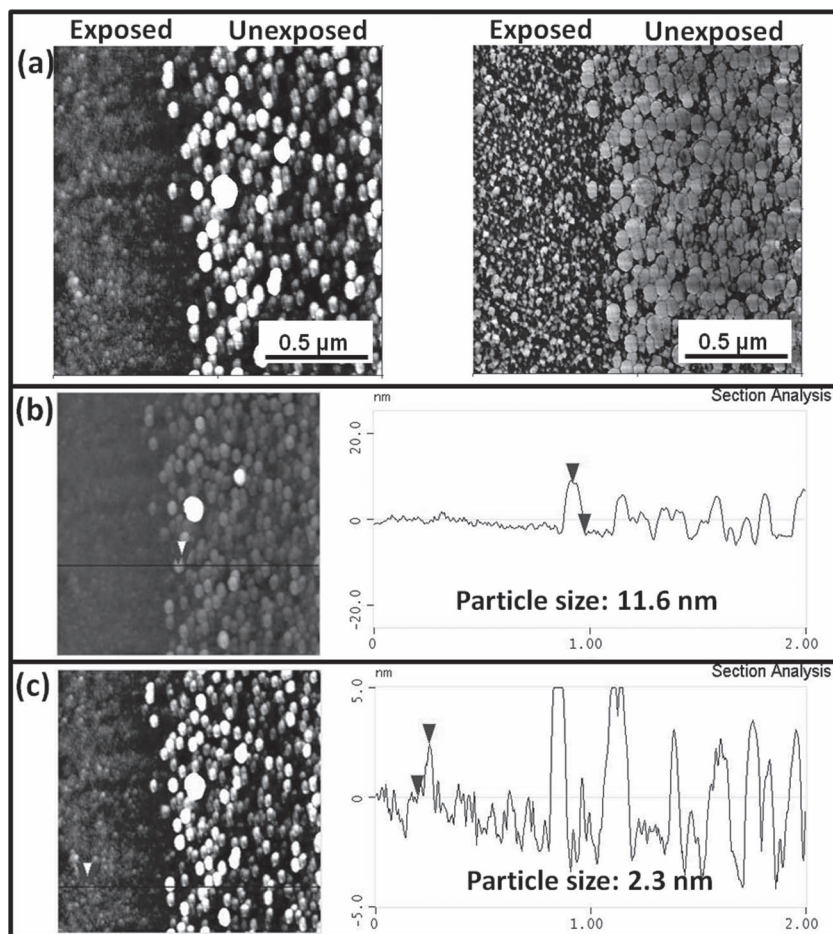


Figure 6. High-resolution AFM image showing the difference between the laser-exposed and unexposed areas of silver film. a) Topography (left; z-scale: 10 nm) and phase (right; z-scale: 60°). Sectional analysis showing the height variation in the b) unexposed areas and c) exposed areas.

2.6. Local Temperature Estimation

Figure 7 shows the morphology of the silver film annealed at different temperatures. It can be seen that the surface morphology of the silver film remains unaltered on annealing up to 450 °C, with a uniform particle size distribution over the entire surface. Annealing above this temperature results in an increase in the lateral dimensions of the silver nanoparticles with the height decreasing to 7.3 ± 1.1 nm. These changes suggest that the silver nanoparticles melt upon annealing above 450 °C. Thus, exposing the substrate to the highest temperature results in local melting causing the silver nanoparticles to aggregate and grow in size. On the contrary, in case of the sputtered silver film exposed to the laser source, the particles are in a state of confinement in the exposed areas and account for the excess temperature by the reduction of size and increasing specific surface area. It is logical to assume that the temperature required for bringing

about a change in morphology of silver nanoparticles would be similar for thermal-based annealing and laser-based transformation. To further confirm this independently, thin films of common polymers, such as poly(4-vinylphenol), with a well known thermal decomposition temperature above 360 °C,^[64] were deposited on noble metal substrates and exposed to the laser under identical conditions. As a result, we observed an intense and highly localized thermal decomposition of a 100 nm thin film of the selected polymers deposited on silver substrate in areas exposed to the laser, whereas the morphology remained unaffected for a similar polymer film deposited on silicon. Such thermal decomposition additionally confirms a localized plasmon-assisted laser-induced thermal heating on the silver surface with a temperature well exceeding 360 °C.

2.7. Application of Laser-Induced Phase Transformation of Carbon on a Copper Substrate

As a proof of concept experiment, we studied the effect of laser exposure on the physical state of the carbon deposits fabricated on top of a copper substrate, which is a commonly used material in the semiconductor industry. **Figure 8a** shows the morphology of the copper substrate along with the corresponding cross-sectional analysis. Similar to the silver substrate, the copper substrate also showed the presence of a granular surface topography with a particle size of 9.4 ± 0.6 nm. Further,

on measuring the optical properties of the copper film, it was observed that the refractive index of the film approaches a minimum between 460 and 500 nm, corresponding to the free

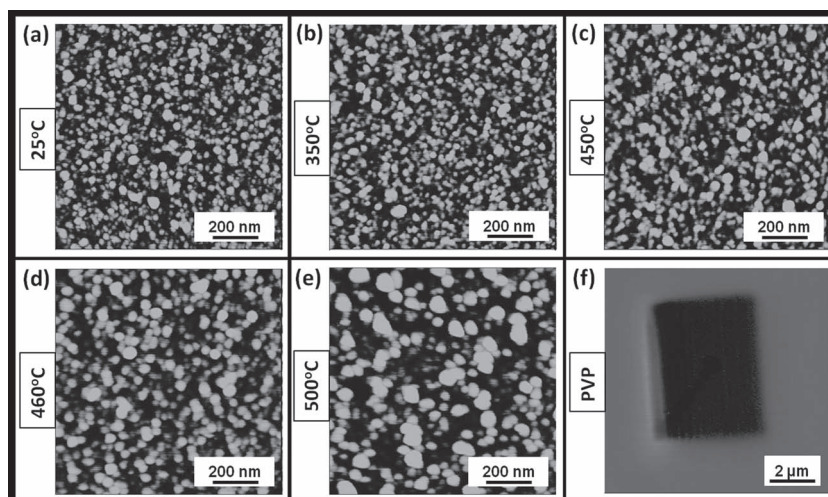


Figure 7. High-resolution AFM image showing the morphology of silver film at different temperatures. The z-scale is 10 nm for all images.

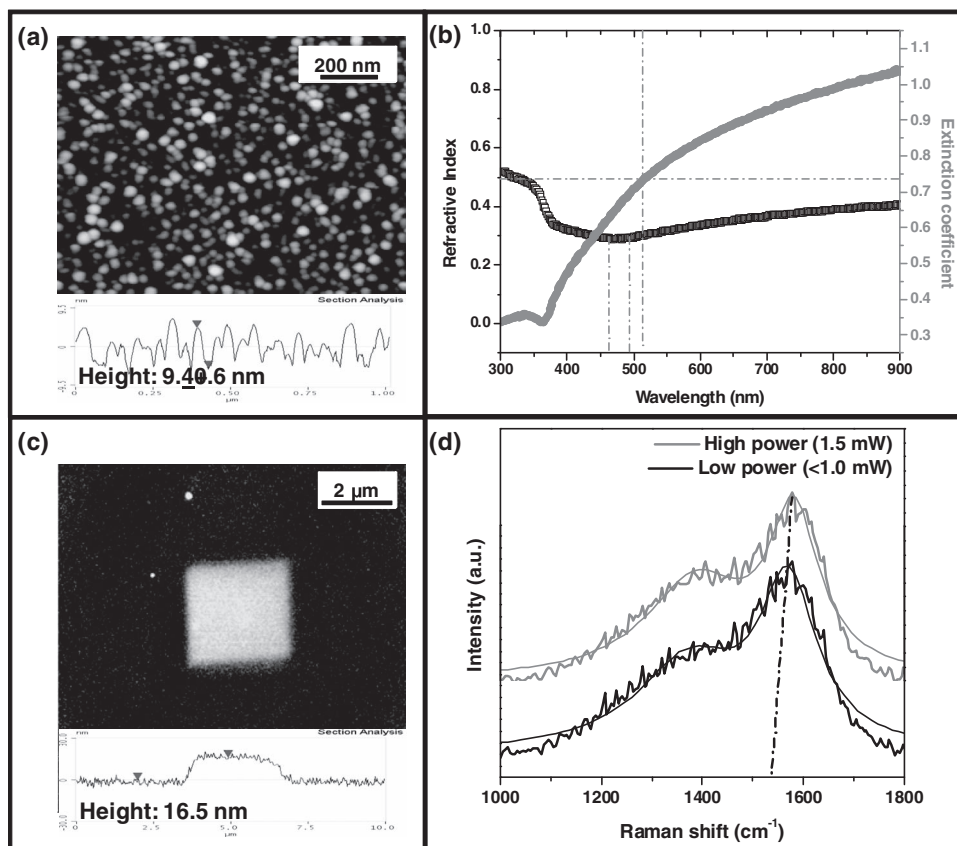


Figure 8. a) Morphology of the copper film showing granular morphology along with the cross-sectional profile (z-scale: 20 nm). b) The variation of refractive index (n) and absorption coefficient (k) with wavelength of copper film. c) Topography of the EBID carbon square deposited on the copper film along with the cross-sectional profile (z-scale: 40 nm). d) Raman spectra of the carbon square at different laser powers. The dotted line indicates the blue shift in the G-band peak position.

electron oscillations of the surface plasmons as a response to the incident electromagnetic radiation (Figure 8b). Thus, the surface plasmon resonance of the copper film was also near the laser excitation wavelength as observed for the gold and silver film.

However, on comparing the extinction coefficient of the copper film with the gold and silver films, it was observed that the copper film absorbs 2.5 times less light than the gold film and 5 times less light than the silver film at a wavelength of 514 nm. Thus, according to the hypothesis presented in the earlier sections, the carbon deposits should not graphitize on the copper film. In order to prove this, we fabricated carbon squares on top of the copper film. Figure 8c shows the morphology of the carbon square along with the corresponding cross-sectional profile. The height of the square was around 16.5 nm with lateral dimensions of $\approx 3 \mu\text{m} \times 3 \mu\text{m}$. Upon exposing the deposit to the Raman laser at 514 nm, it was observed that the deposit showed amorphous behavior, as expected, with a G-band position around 1568 cm^{-1} (Figure 8d).

This suggests that the surface plasmons of the copper film do not absorb enough light at 514 nm to bring about a local increase in the temperature that is high enough for graphitization of the carbon deposit. However, in order to increase the effective absorption of light at 514 nm, the laser power can be increased. Thus, we exposed another carbon square fabricated under similar conditions to the laser source at slightly higher power

($\approx 1.5 \text{ mW}$) and monitored the Raman spectra. It was observed that the G-band peak position blue-shifts towards the graphitic peak position at 1580 cm^{-1} (Figure 8d). This further validates the role of surface plasmons in bringing about a localized phase transition in amorphous carbon deposits upon exposure to light.

2.8. Kinetics of Laser-Induced Phase Transformation

The carbon dots on different metal films were exposed to the laser illumination under minimum power ($<1 \text{ mW}$) for increasing periods of time and spectra were recorded after each exposure interval to monitor kinetics of phase transformation. Figure 9 shows the variation of G-band peak position and the D/G ratio for the dots deposited on silver and gold films. It can be seen that initially the deposits are amorphous with the G-band peak position around 1558 cm^{-1} and 1567 cm^{-1} on gold and silver films, respectively (Figure 9a). Also, the D/G ratio for deposits occurs around 0.8 on gold and 1.2 on silver films (Figure 9b). As

the exposure time increases, the G-band peak position for carbon deposits on silver films steadily increases and reaches 1580 cm^{-1} after $\approx 30 \text{ s}$ of light exposure with the D/G ratio increasing to 1.6. Further increase in the exposure time results in the steady shift of G-band peak position towards 1590 cm^{-1} , suggesting the formation of a nanocrystalline graphitic phase.^[37] Thus, the carbon deposits on the silver film undergo a rapid (tens of seconds) transition from amorphous to graphitic to nanocrystalline graphitic phase upon exposure to the laser source (Figure 9c).

The G-band peak position of deposits on gold films shows a sharp increase up to 1572 cm^{-1} during the initial exposure followed by a plateau region (Figure 9). This minor shift suggests that the carbon deposits on gold undergo only partial graphitization to disordered graphitic phase, without a complete transformation. The D/G ratio of carbon deposits on gold film remains about constant around 0.9 (Figure 9).

2.9. Changes in the Electronic Properties of Carbon Deposits Upon Laser Illumination

In order to address the practical applications of the amorphous to graphitic phase transformation in controlling the electrical properties of carbon/metal interfaces, we performed CFM

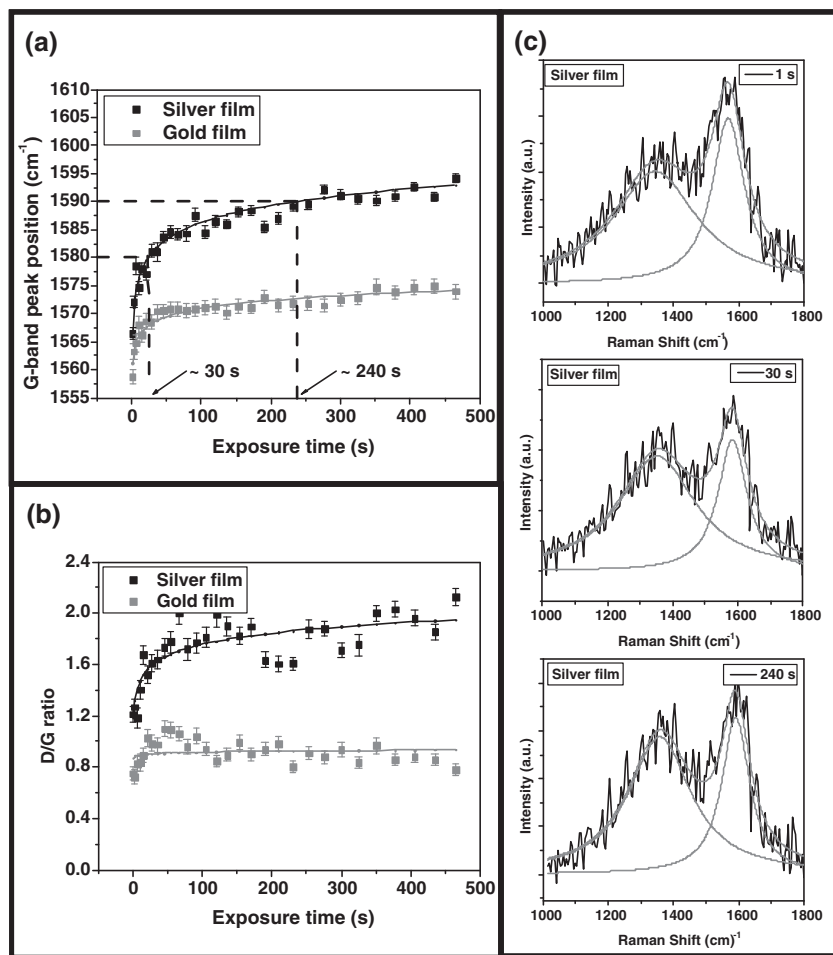


Figure 9. Kinetics of phase transformation of the carbon deposit on different metal films on exposure to 514 nm laser source. a) G-band peak position of the carbon deposit at different exposure times. The solid lines represent a fit to the data points. b) Corresponding D/G ratio. The solid lines represent a fit to the data points. c) Raman spectra of the carbon deposit on silver at different time intervals.

measurements of laser-exposed amorphous carbon deposits. An electrically biased metal-coated tip rasters across the surface of the carbon deposits and the current flowing through the system is recorded.^[68] The current flow will thus depend on the contact resistance between the tip and the surface and the resistance of the material itself. In order to have a valid comparison between the amorphous and graphitic domains, we used the same tip to scan both areas within the same sample. However, the shape of the dots is not ideal for such measurements because the pillar-like morphology can be easily destroyed by the relatively large forces used during the CFM scanning process. Therefore, we used square carbon deposits for CFM experiments.

As a control, we fabricated square carbon deposits on a silicon substrate and exposed a small area (1 $\mu\text{m} \times 1 \mu\text{m}$) of it to the laser operated under minimum power (<1 mW). Upon analyzing the morphology of the deposit after the laser exposure, it was observed that the laser locally ablates the exposed area of the deposit (Figure 10a,b). However, sectional analysis reveals that a significant layer of the deposit (≈ 35 nm) still remains separated from the underlying silicon substrate (Figure 10c).

The phase image show similar features in the exposed and unexposed area, further suggesting the absence of phase transition in the carbon deposits on silicon exposed to the laser source.

Similarly, Figure 11a shows the amplitude (morphology) and phase (stiffness) of EBID square carbon deposit on a gold film for CFM experiments. It can be seen that the carbon square shows some non-uniformity in its thickness with its center being higher than the periphery, with the height of the square ≈ 32 nm at the center. Inside the square, a smaller dark square can be seen, which represents the surface area that was exposed to laser illumination under similar conditions as before. High-resolution AFM imaging around the exposed region shows that the laser ablates a part of the deposit (Figure 11b). The laser exposure resulted in the ablation of the deposit forming a crater up to 20 nm deep. This suggests the oxidation of sp³ carbon from the deposit. However, a thin layer of the material (≈ 12 nm) still remains intact after exposure to laser irradiation. The phase image also reveals the formation of an area with different surface properties within the exposed region (Figure 11c).

Figure 12a shows the topographical features of the EBID square carbon deposit on a silver film, which are similar to those observed on the gold film. Exposure to the laser illumination resulted in the ablation of the carbon deposit with initial thickness of 35 nm (dark square at the center). High-resolution AFM images near the exposed areas reveal changes in morphology of the initially amorphous carbon (Figure 12b). The laser exposure resulted in a significant reduction in its size

due to material ablation with a residual (≈ 13 nm) carbon film left within the laser exposed "crater". The phase image shows the formation of carbon material with different physical structure in the areas exposed to the laser beam (Figure 12c). This similarity suggests that the laser exposure has similar effect on the morphology of the amorphous carbon deposits on different substrates.

According to the arguments put forth earlier based upon the Raman scattering studies, it is expected that the areas exposed to the laser irradiation would consist of disordered and nanoscale graphitic domains (conductive) while the remaining film should consist of amorphous carbon (insulating). The CFM images were obtained by maintaining a minimum force between the tip and the sample in order to prevent any structural damage to the deposits as the tip moved across the surface. Multiple scans over the laser-exposed areas were performed and analyzed for the changes in the morphology and dimensions during the scanning process. Sectional profile analysis showed a negligible change in structure of the deposits during imaging.

Figure 13 shows the conductivity map of these deposits on different metal films obtained via CFM. The deposit on

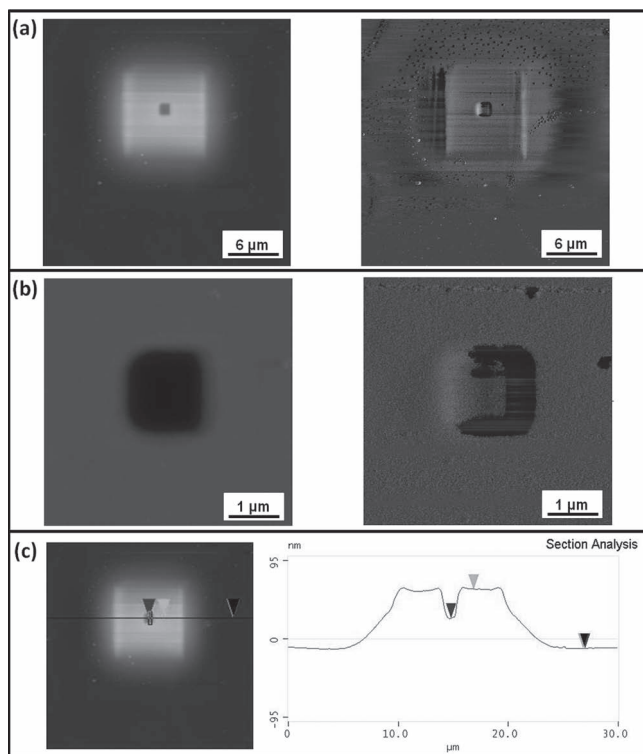


Figure 10. Morphology of amorphous carbon square on a silicon substrate. a) Topography (z-scale: 200 nm) and the corresponding phase (z-scale: 60°) showing the square and the laser-exposed area at the center, b) high-resolution topography (z-scale: 100 nm) and phase (z-scale: 60°) of the laser-exposed areas showing the difference in morphology, and c) sectional analysis of the laser-exposed area.

the gold film shows much improved conductivity at the laser exposed areas. However, the surrounding area shows practically no current flow, i.e., carbon film remains nearly insulating. Exact values of the resistance cannot be obtained quantitatively because of the unknown contact resistance. However, qualitatively the CFM images clearly identify the graphitic and amorphous domains and degree of graphitization. Moreover, the area of amorphous carbon exposed to the laser on the silver film shows a much greater electrical conductivity (Figure 13b, current of ≈ 0.5 mA flows from the CFM tip to the substrate on applying a sample bias of 3.0 V) as compared to the deposits on gold film (Figure 13a, current of ≈ 0.5 nA flows from the CFM tip to the substrate on applying a sample bias of 9.0 V).

It is difficult to estimate or compare the electrical conductivity of the amorphous carbon in the unexposed areas of the square deposit since it shows no measurable current even after applying a maximum sample bias of 10 V. However, since the amorphous carbon maintains its identity in the unexposed areas, irrespective of the underlying substrate, it can be said that the electrical conductivity of amorphous carbon is significantly lower than that of partially graphitized carbon on the gold film. The electrical conductivities of gold (4.2×10^7 S m^{-1}) and silver (6.2×10^7 S m^{-1}) are large and almost identical at room temperature.^[65] Thus, assuming the contact resistance between the sample and the tip to be same in both cases, the

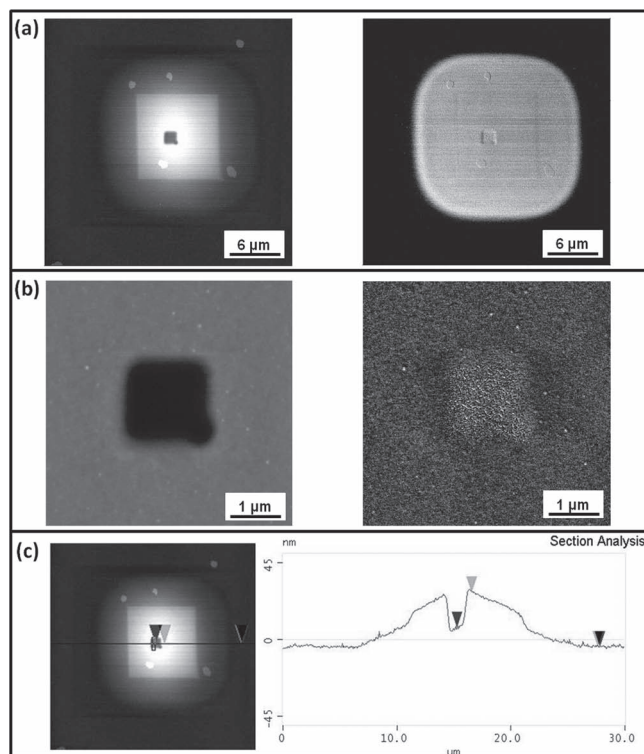


Figure 11. Morphology of amorphous carbon square on gold film. a) Topography (z-scale: 100 nm) and the corresponding phase (z-scale: 90°) showing the square and the laser-exposed area at the center. b) High-resolution topography (z-scale: 50 nm) and phase (z-scale: 30°) of the laser-exposed areas showing the difference in morphology and c) sectional analysis of the laser-exposed area.

presence of the silver film resulted in an increase in the electrical conductivity by over seven orders of magnitude (resistance of the laser exposed carbon film is ≈ 0.6 k Ω s on the silver substrate, compared to ≈ 14 G Ω s on the gold substrate) and, thus, much improved overall electrical conductivity (or dramatically decreased resistivity) at the carbon/silver interface after laser-induced transformation.

3. Conclusions

We have shown that a localized and confined change in phase and electrical properties occurs in the EBID amorphous carbon nanostructures deposited on top of nanostructured metal films upon exposure to the laser illumination. Microscopic amorphous carbon deposits on silicon, gold, and silver showed different structural characteristics upon laser exposure. Specifically, the amorphous carbon deposits maintained their character under laser illumination on a silicon substrate but showed partial and full graphitization on gold and silver films. This change in the material properties is attributed to the local laser-induced heating of the metal nanoparticles with a close match of the light absorption frequency with the laser wavelength. We demonstrated that the phase transformation of carbon can also be brought about on substrates such as copper, which has a low light absorptive

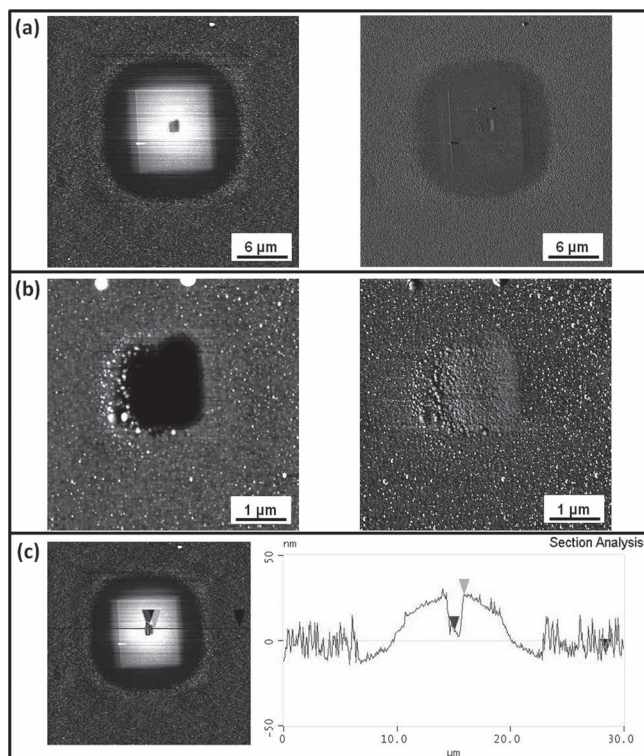


Figure 12. Morphology of amorphous carbon square on silver film. a) Topography (z-scale: 100 nm) and the corresponding phase (z-scale: 90°) showing the square and the laser-exposed area at the center. b) High-resolution topography (z-scale: 50 nm) and phase (z-scale: 30°) of the laser-exposed areas showing the difference in morphology and c) sectional analysis of the laser-exposed area.

index, by tuning the incident laser intensity. Such transformation resulted in dramatic increases in the electrical conductivity of the amorphous carbon deposits. We suggest that the surface plasmons assist in converting the incident light energy into heat that enables a localized phase transition in the amorphous carbon nanostructures to nanocrystalline carbon. Localized graphitization of nanoscale amorphous carbon deposits can be important in applications where low temperature, localized, and fast carbon–metal interconnect fabrication are key issues.

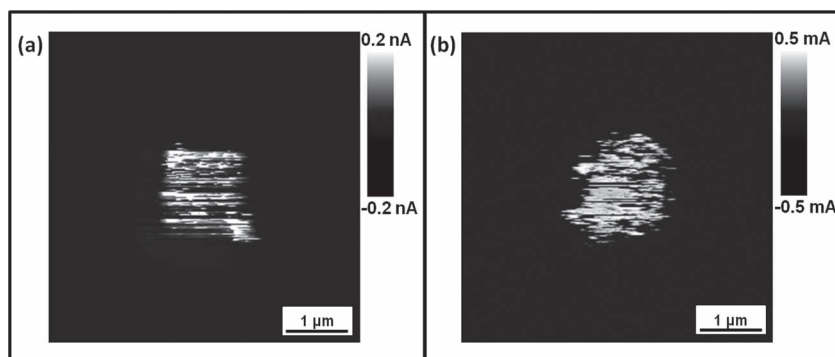


Figure 13. CFM imaging of the deposit on a) gold film and b) silver film, partially exposed to the 514 nm laser.

4. Experimental Section

Substrate Preparation: Silicon (100) wafers were cleaned in piranha solution (3:1 mixture of $\text{H}_2\text{SO}_4/\text{H}_2\text{O}_2$, hazardous solution) for 1 h and then rinsed thoroughly with Nanopure water (18 M Ω cm).^[66] Gold and silver were sputtered on the cleaned silicon substrates for 2 min and copper was sputtered for 10 min at a 30% setpoint in a Denton Vacuum Desk IV sputterer under an argon atmosphere at a pressure of 50 mbar. The average thicknesses of the gold, silver, and copper films as measured from ellipsometry were 14.4 ± 0.2 nm, 10.2 ± 0.18 nm, and 17.0 ± 0.12 nm, respectively.

Residual hydrocarbons and acetone were used as sources of the precursor molecules to induce the growth of carbon deposits over the substrates mentioned in the earlier section.^[22,23,25] EBID carbon deposits were fabricated using a Quanta 200 ESEM operated under 0.01 Pa. The cone-shaped carbon deposits shown in Figure 2 were deposited by keeping the electron beam in spot mode for a period of 10 min. An electron beam energy of 25 keV with the electron beam current in the ≈ 20 pA (spot size 3) was used for deposition. The square carbon deposits shown in Figure 9–11 were made by scanning the electron beam at an energy of 25 keV and current of ≈ 250 pA (spot size 5), using the NPGS (Nanometer Pattern Generation System) program with 1300 mC cm⁻² of electron beam area dose. In order to keep the thickness of the squares similar, the deposition time per square was 45 min and 90 min on the gold and silver films, respectively. Silver films shown in Figure 7 were annealed in a Barnstead Thermolyne furnace for 5 s at different temperatures under normal atmospheric conditions.

Characterization: AFM topographical and phase images were collected with a Dimension-3000 microscope, using silicon tips with tip radii between 10 and 20 nm and a spring constant of about 40 N m⁻¹, in accordance with previously reported procedures.^[67,68] The samples were scanned at 0.5–1.0 Hz. The domain height and surface area coverage were determined from cross-sectional and bearing analysis, respectively.

Raman data were obtained using a WITec (Alpha 300R) confocal Raman microscope using Ar ion laser (514.5 nm) as an excitation source.^[69] The images were obtained by scanning an area of 5 $\mu\text{m} \times 5 \mu\text{m}$ for the dots and 1 $\mu\text{m} \times 1 \mu\text{m}$ for the square with a 100 \times objective (Olympus 100 \times -NA (numerical aperture) = 0.9). The spectra were obtained under minimum laser power (<1 mW) to avoid any laser-induced annealing, as verified independently. The integration time was optimized at 1 s for the all the deposits in order to obtain higher signal-to-noise ratio. The spectra were integrated between 1000 cm⁻¹ and 1800 cm⁻¹ to account for the D-band and G-band. A grating with 600 grooves mm⁻¹ grating with a spectral resolution of 4 cm⁻¹ was used for this study.

Measurement of the optical properties was carried out using a Woollam M2000U (J.A. Woollam Co., Inc., Lincoln, NE) multiangle ellipsometer with WVASE 32 analysis software for three incident angles (65°, 70°, and 75°).^[70] The psi (polarized angle) and delta (phase) values were measured and fitted with the stored parameters for the gold, silver, and copper model to determine the thickness and optical constants (refractive index (n) and extinction coefficient (k)) of the metal films over wavelengths of 300 nm to 900 nm.

Conductivity maps were collected using Innova AFM microscope (Veeco) using silicon tips with tip radii of 30 nm and a spring constant of about 1–3 N m⁻¹, coated with 20 nm Pt/Au. The samples were scanned at 0.3–0.5 Hz. The sample bias was varied from 1.0 V to 10 V and the amplifier gains were varied from 10³ V A⁻¹ to 10⁹ V A⁻¹ depending on the substrate.

Acknowledgements

The authors would like to thank Dr. Konrad Rykaczewski for useful discussions. This work was supported by the Semiconductor Research

Corporation (GRC Grant 2008OJ1864.1281) and the NSF Grant DMI 0403671.

Received: November 5, 2011

Revised: December 16, 2011

Published online: February 27, 2012

- [1] *Oxford Dictionary of Biochemistry and Molecular Biology*, (Eds: A. D. Smith, S. P. Dutta, G. Howard Smith, P. N. Campbell, R. Bentley, H. A. McKenzie, D. A. Bender, A. J. Harris, T. W. Goodwin, J. H. Parish, S. C. Parfith), Oxford University Press, Oxford **1997**.
- [2] D. A. Bryant, N. U. Frigaard, *Trends Microbiol.* **2006**, *14*, 488.
- [3] D. H. Waldeck, *Chem. Rev.* **1991**, *91*, 415.
- [4] J. P. Fouassier, *Photoinitiation, Photopolymerization, and Photocuring: Fundamentals and Applications*, Hanser Publishers, Munich **1995**.
- [5] J. Berkowitz, *Photoabsorption, Photoionization, and Photoelectron Spectroscopy*, Academic Press, New York **1979**.
- [6] S. M. Ryvkin, *Photoelectric Effects in Semiconductors*, Consultants Bureau, New York **1964**.
- [7] W. M. Fisher, S. C. Rand, *J. Appl. Phys.* **2011**, *109*, 064903.
- [8] A. Rosencwaig, *Photoacoustics and Photoacoustic Spectroscopy*, Wiley, New York **1980**.
- [9] D. P. Almond, P. M. Patel, *Photothermal Science and Techniques*, Chapman & Hall, London **1996**.
- [10] P. K. Jain, X. Huang, I. H. El-Sayed, M. A. El-Sayed, *Acc. Chem. Res.* **2008**, *41*, 1578.
- [11] R. Elghain, J. J. Storhoff, R. C. Mucic, R. L. Letsinger, C. A. Mirkin, *Science* **1997**, *277*, 1078.
- [12] A. J. Haes, R. P. Van Duyne, *J. Am. Chem. Soc.* **2002**, *124*, 10596.
- [13] L. R. Hirsch, R. J. Stafford, J. A. Bankson, S. R. Sershen, B. Rivera, R. E. Price, J. D. Hazle, N. J. Halas, J. L. West, *Proc. Natl. Acad. Sci. USA* **2003**, *100*, 13549.
- [14] A. Sidorenko, C. Houphouet-Boigny, O. Villavicencio, M. Hashemzadeh, D. V. McGrath, V. V. Tsukruk, *Langmuir* **2000**, *16*, 10569.
- [15] L. Cao, D. N. Barsic, A. R. Guichard, M. L. Brongersma, *Nano Lett.* **2007**, *7*, 3523.
- [16] A. Nitzan, L. E. Brus, *J. Chem. Phys.* **1981**, *75*, 2205.
- [17] K. G. Stamplecoskie, N. L. Pacioni, D. Larson, J. C. Scaiano, *J. Am. Chem. Soc.* **2011**, *133*, 9160.
- [18] P. K. Jain, I. H. El-Sayed, M. A. El-Sayed, *Nano Today* **2007**, *2*, 18.
- [19] M. Hu, J. Chen, Z. Li, L. Au, G. V. Hartland, X. Li, M. Marquez, Y. Xia, *Chem. Soc. Rev.* **2006**, *35*, 1084.
- [20] Z. Wei, D. Wang, S. Kim, S. Y. Kim, Y. Hu, M. K. Yakes, A. R. Laracuenta, Z. Dai, S. R. Marder, C. Berger, W. P. King, W. A. de Heer, P. E. Sheehan, E. Riedo, *Science* **2010**, *328*, 1373.
- [21] S. J. Randolph, J. D. Fowlkes, P. D. Rack, *Crit. Rev. Solid State Mater. Sci.* **2006**, *31*, 55.
- [22] K. Rykaczewski, O. J. Hilderth, D. D. Kulkarni, M. R. Henry, S. K. Kim, C. P. Wong, V. V. Tsukruk, A. G. Fedorov, *ACS Appl. Mater. Interfaces* **2010**, *2*, 969.
- [23] D. D. Kulkarni, K. Rykaczewski, S. Singamaneni, S. K. Kim, A. G. Fedorov, V. V. Tsukruk, *ACS Appl. Mater. Interfaces* **2011**, *3*, 710.
- [24] F. Banhart, *Nano Lett.* **2001**, *1*, 329.
- [25] K. Rykaczewski, M. R. Henry, S. K. Kim, A. G. Fedorov, D. D. Kulkarni, S. Singamaneni, V. V. Tsukruk, *Nanotechnology* **2010**, *21*, 035202.
- [26] B. Marchon, N. Heiman, M. R. Khan, A. Lautie, J. W. Ager, D. K. Veirs, *J. Appl. Phys.* **1991**, *69*, 5748.
- [27] P. Zhang, B. K. Tay, C. Q. Sun, S. P. Lau, *J. Vac. Sci. Technol. A* **2002**, *20*, 1390.
- [28] M. G. Beghi, A. C. Ferrari, K. B. K. Teo, J. Robertson, C. E. Botani, A. Libassi, B. K. Tanner, *Appl. Phys. Lett.* **2002**, *81*, 3804.
- [29] S. J. Bull, *Diamond Relat. Mater.* **1995**, *4*, 827.
- [30] W. S. Choi, B. Hong, *Renewable Energy* **2008**, *33*, 226.
- [31] P. M. Ajayan, M. Terrones, A. de la Guardia, V. Huc, N. Grobert, B. Q. Wei, H. Lezec, G. Ramanath, T. W. Ebbesen, *Science* **2002**, *296*, 705.
- [32] S. Osswald, K. Behler, Y. Gogotsi, *J. Appl. Phys.* **2008**, *104*, 074308.
- [33] M. A. El-Sayed, *Acc. Chem. Res.* **2001**, *34*, 257.
- [34] L. Rontzsch, K. H. Heinig, J. A. Schuller, M. L. Brongersma, *Appl. Phys. Lett.* **2007**, *90*, 044105.
- [35] A. O. Govorov, W. Zhang, T. Skeini, H. Richardson, J. Lee, N. A. Kotov, *Nanoscale Res. Lett.* **2006**, *1*, 84.
- [36] B. F. Soares, F. Johnson, N. I. Zheludev, *Phys. Rev. Lett.* **2007**, *98*, 153905.
- [37] A. C. Ferrari, J. Robertson, *Philos. Trans. R. Soc. A* **2010**, *362*, 2477.
- [38] F. Tuinstra, J. L. Koenig, *J. Chem. Phys.* **1970**, *53*, 1126.
- [39] R. J. Nemanich, S. A. Solin, *Phys. Rev. B* **1979**, *20*, 392.
- [40] *Properties of Amorphous Carbon*, INSPEC, (Ed. S. R. P. Silva), Institute of Engineering Technology, Herts, UK **2003**.
- [41] N. R. Raravikar, P. Keblinski, A. M. Rao, M. S. Dresselhaus, L. S. Schadler, P. M. Ajayan, *Phys. Rev. B* **2002**, *66*, 235424.
- [42] L. S. Schadler, S. C. Giannaris, P. M. Ajayan, *Appl. Phys. Lett.* **1998**, *73*, 3842.
- [43] L. Ci, Z. Zhou, L. Song, X. Yan, D. Liu, H. Yuan, Y. Gao, J. Wang, L. Liu, W. Zhou, G. Wang, S. Xie, *Appl. Phys. Lett.* **2003**, *82*, 3098.
- [44] F. C. Marques, R. G. Lacerda, A. Champi, V. Stolojan, D. C. Cox, S. R. P. Silva, *Appl. Phys. Lett.* **2003**, *83*, 3099.
- [45] A. C. Ferrari, B. Kleinsorge, N. A. Morrison, A. Hart, V. Stolojan, J. Robertson, *J. Appl. Phys.* **1999**, *85*, 7191.
- [46] S. B. Cronin, A. K. Swan, M. S. Unlu, B. B. Goldberg, M. S. Dresselhaus, M. Tinkham, *Phys. Rev. B* **2005**, *72*, 035425.
- [47] C. Jiang, H. Ko, V. V. Tsukruk, *Adv. Mater.* **2005**, *17*, 2127.
- [48] A. Onodera, Y. Irie, K. Higashi, J. Umemura, T. Takenaka, *J. Appl. Phys.* **1991**, *69*, 2611.
- [49] R. S. Sennett, G. D. Scott, *J. Opt. Soc. Am.* **1950**, *40*, 203.
- [50] U. Kreibig, M. Vollmer, *Optical Properties of Metal Clusters*, Springer, Berlin **1995**.
- [51] P. K. Jain, M. A. El-Sayed, *Chem. Phys. Lett.* **2010**, *487*, 153.
- [52] A. I. Maarroof, M. B. Cortie, G. B. Smith, *J. Opt. A: Pure Appl. Opt.* **2005**, *7*, 303.
- [53] M. C. Dixon, T. A. Daniel, M. Hieda, D. M. Smilgies, M. H. W. Chan, D. L. Allara, *Langmuir* **2007**, *23*, 2414.
- [54] B. Liedberg, C. Nylander, I. Lundstrom, *Sens. Actuators* **1983**, *4*, 299.
- [55] H. H. Ko, S. Singamaneni, V. V. Tsukruk, *Small* **2008**, *4*, 1576.
- [56] P. K. Jain, X. Huang, I. H. El-Sayed, M. A. El-Sayed, *Plasmonics* **2007**, *2*, 107.
- [57] A. O. Govorov, H. H. Richardson, *Nano Today* **2007**, *2*, 30.
- [58] H. H. Richardson, M. T. Carlson, P. J. Tandler, P. Hernandez, A. O. Govorov, *Nano Lett.* **2009**, *9*, 1139.
- [59] G. Baffou, R. Quidant, C. Girard, *Appl. Phys. Lett.* **2009**, *94*, 153109.
- [60] P. V. Kamat, M. Flumiani, G. V. Hartland, *J. Phys. Chem. B* **1998**, *102*, 3123.
- [61] A. Takami, H. Kurita, S. Koda, *J. Phys. Chem. B* **1999**, *103*, 1226.
- [62] F. Stietz, *Appl. Phys. A: Mater. Sci. Process* **2001**, *72*, 381.
- [63] N. V. Tarasenko, A. V. Butsen, E. A. Nevar, *Appl. Surf. Sci.* **2005**, *247*, 410.
- [64] Poly (4-vinyl phenol), Sigma-Aldrich database, http://www.sigmaaldrich.com/catalog/ProductDetail.do?D7=0&N5=SEARCH_CONCAT_PNO|BRAND_KEY&N4=436224|ALDRICH&N25=0&QS=ON&F=SPEC (accessed October 2011).
- [65] A. M. Russell, K. L. Lee, *Structure-Property Relations in Nonferrous Metals*, John Wiley & Sons Inc., Hoboken, NJ **2005**.
- [66] N. B. Sheller, S. Petrash, M. D. Foster, V. V. Tsukruk, *Langmuir* **1998**, *14*, 4535.
- [67] V. V. Tsukruk, *Rubber Chem. Technol.* **1997**, *70*, 430.
- [68] M. E. McConney, S. Singamaneni, V. V. Tsukruk, *Polym. Rev.* **2010**, *50*, 235.
- [69] S. Singamaneni, M. K. Gupta, R. Yang, M. Tomczak, R. R. Naik, Z. L. Wang, V. V. Tsukruk, *ACS Nano* **2009**, *3*, 2593.
- [70] *Handbook of Ellipsometry*, (Eds: H. G. Tompkins, E. A. Irene), Springer Science & Business, New York **2005**.